AGU PUBLICATIONS

JGR

Journal of Geophysical Research: Oceans

RESEARCH ARTICLE

10.1002/2013JC009422

Key Points:

- MJO excites systematic anomalies in MLD but not BLT
- Zonal advection dominates MJO salinity anomalies at 90°E, 0°N
- When the barrier layer is thin, the MJO excites stronger SST anomalies

Correspondence to:
K. Drushka,
kdrushka@ucsd.edu

Citation:
Drushka, K., J. Sprintall, and S. T. Gille (2014), Subseasonal variations in salinity and barrier-layer thickness in the eastern equatorial Indian Ocean, *J. Geophys. Res. Oceans*, *119*, 805–823, doi:10.1002/2013JC009422.

Received 11 SEP 2013
Accepted 8 JAN 2014
Accepted article online 16 JAN 2014
Published online 7 FEB 2014

Subseasonal variations in salinity and barrier-layer thickness in the eastern equatorial Indian Ocean

Kyla Drushka[1], Janet Sprintall[1], and Sarah T. Gille[1]

[1]Scripps Institution of Oceanography, University of California, San Diego, California, USA

Abstract The barrier layer, the layer between the bottom of the density-defined mixed layer and the isothermal layer in the upper ocean, may play a role in air-sea dynamics. In the present study, data from Argo profiling floats in the tropical Indian Ocean and a mooring at 90°E, 0°N are used to examine subseasonal variations in upper ocean salinity and barrier-layer thickness (BLT) during boreal winter. In the eastern equatorial Indian Ocean, subseasonal variations in BLT are energetic. However, composites used to isolate the Madden-Julian Oscillation (MJO) component of the subseasonal signal reveal that, on average, the MJO anomaly in BLT is negligible despite large swings in both the mixed-layer depth and the isothermal-layer depth. This discrepancy is likely due to (a) noise from other subseasonal processes; and (b) the diversity of individual MJO events: the thickness of the mixed layer and the isothermal layer are sensitive to wind and rain forcing, so even subtle differences in the phasing and strength of MJO-related atmospheric anomalies can produce a very different effect on upper ocean stratification and hence on the thickness of the barrier layer. The effect of the barrier layer on the upper ocean response to MJO forcing is also evaluated. When the barrier layer is thick, entrainment cooling during the MJO is reduced, so the MJO drives a weaker sea surface temperature anomaly. This suggests that modulation of BLT can have significant consequences for the response of the upper ocean to the MJO, and hence, potentially, for feedbacks of the ocean onto the atmosphere on MJO time scales.

1. Introduction

Subseasonal oceanic and atmospheric variability in the eastern equatorial Indian Ocean (EEIO) is strong, arising from processes that include the Madden-Julian Oscillation (MJO), monsoon active-break activity [*Vecchi and Harrison*, 2002], quasi-biweekly Yanai waves [*Miyama et al*., 2006], and synoptic and mesoscale atmospheric disturbances. The MJO dominates the 30–60 day component of the subseasonal band [*Madden and Julian*, 1994], and has wide-reaching impacts both in terms of its direct impacts on weather [*Hendon et al*., 2000] and its potential interactions with other large-scale phenomena such as monsoons, the El Niño-Southern Oscillation [*Zhang*, 2005], and the Indian Ocean Dipole (IOD) [*Rao and Yamagata*, 2004]. MJO representation in climate models is currently poor [e.g., *Zhang et al*., 2013], and forecast skill is weak [*Gottschalck et al*., 2010]. In part, this is because air-sea coupling in models is difficult to get right: complex feedbacks between the ocean and atmosphere exist on numerous time and space scales, which pose challenges for modeling these processes. An accurate understanding of how the MJO affects upper ocean stratification, and how stratification affects the MJO, is needed in order to accurately represent the MJO in models. This is all the more important in the EEIO, where sea surface temperature (SST) is close to the necessary threshold for deep atmospheric convection [e.g., *Graham and Barnett*, 1987], so small errors in temperature can potentially induce significant uncertainties in how the MJO modulates convection and winds.

One large gap in our understanding of this system is the role that the barrier layer plays in MJO dynamics in the EEIO. In regions where upper ocean stratification is controlled by salinity, a “barrier layer” can exist between the base of the mixed layer and the thermocline [*Lukas and Lindstrom*, 1991; *Sprintall and Tomczak*, 1992]. Barrier layers can affect SST in a number of ways, and have been shown to play an important role in Indian Ocean air-sea dynamics. For example, an anomalously thin barrier layer appears to be an important factor in the onset of IOD events [*Annamalai et al*., 2003; *Masson et al*., 2003; *Qiu et al*., 2012].

While a handful of studies have examined EEIO barrier-layer dynamics on seasonal and longer time scales [e.g., *Masson et al*., 2002; *Qu and Meyers*, 2005; *Agarwal et al*., 2012], to our knowledge, there have been no observational studies considering subseasonal barrier-layer dynamics in the EEIO. The MJO excites substantial anomalies both in the thermohaline [*Matthews et al*., 2010] and the dynamical [*Webber et al*., 2010] properties of the water column, which means that it has the potential to modulate the thickness of the barrier layer. However, measuring the barrier-layer thickness requires temperature and salinity measurements with high vertical resolution (e.g., better than 10 m sampling throughout the thermocline) [*Sato et al*., 2006], which has historically been a challenge. In the present study, we use in situ observations from Argo profiling floats to examine subseasonal salinity and barrier-layer anomalies in the EEIO. We begin by considering all frequencies within the subseasonal band, which includes the MJO, monsoon-related, quasi-biweekly, synoptic, and diurnal disturbances. We then turn our attention to the MJO component of the subseasonal band, addressing two questions in particular: (1) does the MJO systematically modulate the thickness of the barrier layer? (2) Does the presence or absence of a barrier layer influence the response of the ocean to MJO forcing?

2. Background

2.1. The Barrier Layer

The ocean mixed layer is defined as the surface layer over which the density is effectively constant. In regions where upper ocean salinity stratification is weak, temperature stratification determines the base of the mixed layer, and the mixed-layer depth (MLD) is equal to the isothermal-layer depth (ILD). If salinity dominates upper ocean stratification, MLD can be shallower than ILD and a layer that is well mixed in temperature but not in salinity lies between the two. This is known as the barrier layer [e.g., *Godfrey and Lindstrom*, 1989; *Sprintall and Tomczak*, 1992], so called because it acts as a barrier between the ocean surface layer and the thermocline by restricting both the impact of surface fluxes on the thermocline and the impact of turbulent processes at the base of the mixed layer on the upper layer [*Lukas and Lindstrom*, 1991; *Sprintall and Tomczak*, 1992; *Vialard and Delecluse*, 1998a].

Barrier layers can affect SST via several mechanisms. In the presence of a barrier layer, incoming fluxes of heat and freshwater can be trapped within the mixed layer, reducing their impacts on the thermocline while enhancing their impacts on surface temperature and salinity. Similarly, by trapping momentum input from winds, barrier layers can also enhance surface currents, and hence horizontal advection. Finally, a barrier layer reduces the vertical temperature gradient at the base of the mixed layer and so can shut off turbulent entrainment of cooler water that usually occurs when the mixed layer deepens. Since SST anomalies in tropical regions can modulate winds and convection, barrier layers can thus indirectly affect the atmosphere, which can potentially feed back onto oceanic anomalies [*Godfrey and Lindstrom*, 1989; *Vialard and Delecluse*, 1998a].

Variations in the thickness of the barrier layer are caused by processes that modulate the relative depths of the mixed layer and the isothermal layer. These include upper ocean salinity changes, wind mixing, horizontal and vertical advection, and planetary waves [e.g., *You*, 1995; *Vialard and Delecluse*, 1998a; *Cronin and McPhaden*, 2002; *Qu and Meyers*, 2005; *Mignot et al*., 2007; *Girishkumar et al*., 2011].

In the eastern Indian Ocean west of Sumatra, strong mean precipitation and river runoff maintain a thick ($>$25 m) year-round barrier layer [*Masson et al*., 2002]. On seasonal and interannual time scales, variations in precipitation, Kelvin and Rossby waves, and zonal convergence and its associated downwelling all modulate barrier-layer thickness (BLT) in the EEIO [*Murtugudde and Busalacchi*, 1999; *Masson et al*., 2002; *Annamalai et al*., 2003; *Qu and Meyers*, 2005; *Chowdary et al*., 2009; *Agarwal et al*., 2012]. The barrier layer has a maximum thickness and horizontal extent along the equator during November as a result of seasonal rainfall, which keeps the mixed layer thin, and a semiannual Kelvin wave, which deepens the ILD relative to the MLD [*Qu and Meyers*, 2005]. An anomalously thin seasonal barrier layer may help trigger IOD events by enhancing entrainment of cold water off the Sumatra coast, both directly (by reduction of the “barrier” effect) [*Annamalai et al*., 2003] and indirectly (by accelerating eastward equatorial jets and thus convergence) [*Masson et al*., 2004].

Subseasonal BLT variations are potentially strong in the EEIO as a result of the MJO, which is a coupled system of deep convection and winds that propagates eastward along the equator from the western Indian Ocean to the central Pacific Ocean every ~30–60 days [e.g., *Zhang*, 2005]. The MJO dominates wintertime subseasonal variability in the EEIO [*Zhang*, 2005]. However, subsurface salinity data with sufficient resolution to resolve changes in BLT on MJO time scales have been sparse, so this topic has not been well explored.

2.2.. Madden-Julian Oscillation

The MJO is a highly variable phenomenon: individual events vary in their strength, timing, propagation speed, and trajectory. Though it is often considered to have a 40–50 day period, MJO energy is in fact distributed widely between ~30 and 100 days [*Zhang*, 2005]. The MJO exerts a profound influence on the thermohaline dynamics of the upper ocean by way of anomalies in heat, momentum, and freshwater fluxes. MJO convective cells produce anomalies in turbulent and sensible heat fluxes [e.g., *Woolnough et al*., 2000] as well as in rainfall [*Shinoda et al*., 1998]. MJO wind anomalies are dominantly zonal, with westerly anomalies beneath and to the west of the convective cells and easterly anomalies to the east. Wind anomalies produce turbulent mixing in the upper ocean as well as horizontal advection of temperature and salinity and their gradients. In addition, zonal winds associated with the MJO can force planetary (Kelvin and Rossby) waves, which may be involved in triggering MJO events themselves [*Webber et al*., 2010, 2012]. All of these processes can alter upper ocean stratification and hence potentially the thickness of the barrier layer. Indeed, in situ studies of the western Pacific Ocean have demonstrated that strong intraseasonal westerly wind and precipitation anomalies associated with the passage of an MJO event can produce dramatic anomalies in the barrier layer [e.g., *You*, 1995; *Anderson et al*., 1996; *Cronin and McPhaden*, 2002; *Weller et al*., 2004]. However, these studies only examined a few individual events. A comparison of these studies shows that the strength, duration, and timing of different MJO events varies widely, and it is not clear whether each MJO event alters the barrier layer in the same way. In the present study, we use composite averages of numerous MJO events to evaluate the systematic response of the ocean to MJO forcing, though we note that this approach smooths out some of the signal, particularly for properties that differ strongly between individual events.

2.3. Subseasonal Salinity and Barrier-Layer Anomalies

Although many studies have used observations to examine the SST signal related to the MJO [e.g., *Shinoda et al*., 1998; *Zhang and McPhaden*, 2000; *Duvel et al*., 2004], few have examined salinity. *Matthews et al*. [2010] used in situ salinity observations from Argo floats along with atmospheric reanalysis data to show that composite MJO patterns of surface salinity in the Indian Ocean are largely consistent with precipitation minus evaporation (P-E), suggesting that atmospheric forcing dominates average MJO salinity variations at the ocean surface. *Grunseich et al*. [2011], using MJO composites based on the Simple Ocean Data Assimilation reanalysis product, also showed that P-E largely dominates MJO composite sea surface salinity anomalies, except right on the equator where jets induced by intraseasonal wind anomalies advect freshwater zonally. *Grunseich et al*. [2013] recently used data from the Aquarius satellite to show that precipitation appears to drive sea surface salinity changes in the EEIO on MJO time scales. Using a full model-based MJO salinity budget in the Indian Ocean, *Schiller and Godfrey* [2003] showed that P-E, horizontal advection, and vertical entrainment may all be equally important. Moreover, their relative importance can vary substantially depending on the location and the MJO phase. This has also been shown for the western Pacific Ocean, where a complex combination of processes governs intraseasonal salinity variations [*You*, 1995; *Anderson et al*., 1996; *Vialard and Delecluse*, 1998b].

To our knowledge, the only study to have explicitly considered intraseasonal BLT variations in the EEIO is the modeling study of *Schiller and Godfrey* [2003]. They showed that a barrier layer develops during the suppressed phase of the MJO, when weak winds permit the mixed layer to shoal, and thins when the MLD deepens during the active phase. *Schiller and Godfrey* [2003] emphasized that the BLT variation over individual events (±15 m) is considerably larger than the average variation over the MJO cycle (±8 m).

3. Data and Methodology

3.1. Data Sets

This study is based on data from the Argo profiling float data set. Delayed-mode Argo data from 2000 to 2012 were obtained from the United States Global Ocean Data Assimilation Experiment (USGODAE) repository and were quality-controlled following *Bosc et al*. [2009]. First, data with temperature values out of the range 5–35°C or salinity values out of the range 30–37 psu were removed. Then, profiles were removed if any of the following criteria were met: (1) no data in the upper 5 m; (2) data gaps exceeding 25 m in the top 150 m; (3) density inversions greater than 0.015 kg m^{-3}; (4) positive temperature gradients greater than 0.7°C m^{-1}; (5) temperature inversions stronger than 0.2°C m^{-1}. This eliminated 3853 profiles, or 4.6% of the total. Around 39,000 profiles made during November-April in the eastern tropical Indian Ocean domain

(20°S–20°N, 60°E–120°E) were collected and binned into overlapping 10° longitude × 6° latitude gridboxes; the distribution is shown in Figure 2e. Each Argo float makes a profile from around 5 m depth down to 1000 or 2000 m approximately every 10 days, measuring temperature (T) and salinity (S) with a vertical resolution of $\Delta z \sim 5$ dbar. Each T and S profile was linearly interpolated to a 1 m vertical grid. Following *Sprintall and Tomczak* [1992] and *de Boyer Montégut et al*. [2007], we defined ILD as the depth at which temperature changed by a threshold value of $\Delta T = 0.3$°C relative to the temperature at a reference depth of 5 m. MLD was defined as the depth at which potential density σ_θ changed relative to the reference depth by an amount $\Delta\sigma_\theta$, where $\Delta\sigma_\theta$ was calculated as the potential density change equivalent to the same temperature change at the local salinity:

$$\Delta\sigma_\theta = \sigma_\theta(T_{ref} - \Delta T, S_{ref}, P_o) - \sigma_\theta(T_{ref}, S_{ref}, P_o). \tag{1}$$

In equation (1), T_{ref} and S_{ref} are the temperature and salinity at the 5 m reference depth and P_o is the pressure at the ocean surface. Then, the thickness of the barrier layer was defined as BLT = ILD – MLD. This method of estimating MLD is useful in barrier-layer studies because, in cases for which the salinity stratification is negligible and MLD is controlled by temperature alone, MLD ≈ ILD and the barrier layer collapses to zero.

We also utilized data from an equatorial mooring at 90°E that is part of the Research Moored Array for African-Asian-Australian Monsoon Analysis and Prediction (RAMA) [*McPhaden et al*., 2009] program. This site was selected because the mooring provides upper ocean velocity measurements, allowing us to assess the subsurface ocean dynamics associated with the MJO in the EEIO. The mooring was equipped with 13 temperature sensors in the top 500 m, with 10–20 m resolution in the top 100 m; six salinity sensors at 10 to 40 m vertical spacing in the top 100 m; an Acoustic Doppler Current Profiler (ADCP), which provided horizontal velocities at 10 m depth bins from 40 to 410 m depth; and a Doppler current meter at 10 m depth, which provided near-surface horizontal velocities. The temperature and salinity data are available from 2004 to present, whereas the ADCP time series begins in 2000. The RAMA data were downloaded from NOAA as daily averages of 0.1 Hz (for T and S) or 1 Hz (for currents) measurements. We linearly interpolated all mooring data to a 1 m vertical grid. As for the Argo data, ILD and MLD were estimated from the mooring data using a reference depth of 5 m and a temperature threshold of 0.3°C. Although mooring data have successfully been used to characterize intraseasonal BLT variations in the Bay of Bengal [*Girishkumar et al*., 2011], we found that the 10 to 20 m vertical spacing of the temperature and salinity sensors gave coarse estimates of MLD and ILD, and so variations on scales less than tens of meters were not accurately resolved. In addition, the mooring captured both temperature and salinity of only 10 boreal winter MJO events, which was not adequate for forming a robust statistical average of the subsurface ocean response to MJO forcing. We thus used Argo data for the majority of the present study. To characterize the temperature, salinity, MLD, and ILD variations at the mooring site, we gathered all Argo profiles made within the $\Delta x = 10°$ longitude $\times \Delta y = 6°$ latitude gridbox centered at 90°E, 0°N. For the 2000–2012 boreal winter time period, this gave 1858 profiles (Figure 2f).

To quantify atmospheric forcing at the mooring site, we used a number of gridded, satellite-based data sets. Wind stress data came from TropFlux [*Praveen Kumar et al*., 2012a], a daily, gridded (1° horizontal resolution) product based on QuikSCAT scatterometer winds, which has been shown to perform well at intraseasonal time scales in the tropical Indian Ocean [*Praveen Kumar et al*., 2012b]. Precipitation estimates came from the Tropical Rainfall Measuring Mission (TRMM) 3B42 product, available on a 0.25° × 0.25° daily grid [*Huffman et al*., 2007]. Heat flux and evaporation were from the Objective Analysis Flux (OAFlux) [*Yu and Weller*, 2007] product, which uses satellite-based observations and is available on a daily, 1° × 1° grid. Finally, outgoing longwave radiation (OLR) from the National Oceanic and Atmospheric Administration (NOAA) was used as a proxy for convection [*Liebmann and Smith*, 1996]. The OLR data are available on a 2.5° × 2.5° daily grid from 1974 to present. Each of these atmospheric variables was linearly interpolated in space to the location of the mooring site to estimate local forcing there.

3.2. Filtering

To isolate subseasonal variations, the mean was removed and the background (seasonal plus interannual anomaly) signals were removed from all variables. For any variable X, this can be expressed as $X' = X - \langle X \rangle - \bar{X}$, where $\langle X \rangle$ represents the time-mean, $\bar{X}$ represents the background signal, and X' represents the subseasonal anomaly. The Argo profile data have irregular temporal sampling, so filtering can introduce spurious signals. Instead, we determined the local background signal from a gridded temperature and salinity data set that is based on Argo [*Roemmich and Gilson*, 2009]. This product is available from 2004 to present with monthly time resolution on a $1^\circ \times 1^\circ$ horizontal grid, and has $\sim$10 m vertical resolution in the top 200 m. These monthly gridded T and S data were used to estimate ILD and MLD based on a temperature and density threshold, respectively. Note that since the gridded data are much smoother than the profile data, it is more appropriate to use a larger threshold to define the ILD (see *de Boyer Montégut et al*. [2004], for an explanation); we set the threshold, ΔT, to 0.5°C. The monthly gridded temperature, salinity, MLD and ILD data were low-pass filtered with a 120 day cutoff to obtain the background signal for each variable $(\bar{X})$, which was then projected onto the time and location of each Argo profile using linear interpolation. This gave an estimate of the background $T(z)$, $S(z)$, MLD and ILD, and hence BLT, for each profile, so each profile measurement X could be separated into $\langle X\rangle+\bar{X}+X'$. The analysis was not sensitive to the threshold value used to estimate the seasonal ILD and MLD: a slightly larger or smaller value of ΔT had only the effect of shifting the average ILD and MLD vertically; since the time-mean was removed before compositing, changing ΔT slightly did not affect the values of X'.

For the interpolated satellite data sets and the RAMA mooring data, which have regular temporal spacing, we simply removed the time-mean and the annual and semiannual harmonics and applied a 120 day low-pass filter to isolate the background signal. Note that X' contains all subseasonal variations, including those from intraseasonal variations such as the MJO as well as any other (e.g. diurnal, synoptic, quasi-biweekly, monsoon-related) activity.

3.3. Compositing Procedure

To characterize the response of the ocean to local atmospheric forcing, we used an index of convection at 90°E, 0°N, where wintertime MJO activity is particularly strong [e.g., *Webster*, 2002]. The index (referred to as the "OLR-90E index") was defined by isolating intraseasonal peaks in daily OLR. To extract only the intraseasonal signal from the OLR data, we applied a Lanczos band-pass filter with a 25–120 day window. This window was chosen to retain the broadest possible range of MJO-band activity so as to avoid edge-effects, while excluding all non-MJO signals: quasi-biweekly and synoptic variations have periods shorter than 25 days, and monsoon-related convection is relatively weak on the equator. "MJO events" were defined as having negative peaks in anomalous OLR exceeding -30 W m^{-2}, effectively extracting intraseasonal anomalies in deep convection. The negative OLR peaks defined the zero-lag time for each event; lags from -20 to $+20$ days were then defined in relation to the peaks.

Figure 1 shows composite OLR anomalies throughout the domain at different lags, which were calculated by averaging subseasonal OLR anomalies at each lag. Positive OLR anomalies propagate eastward from the central Indian Ocean from -20 to -8 days lag, when they reach the Maritime Continent; then, negative OLR anomalies (i.e., anomalous convection) are seen in the central Indian Ocean and follow the same eastward trajectory, peaking at 90°E,0°N at lag zero as expected and then continuing eastward and weakening by $+8$ days lag. This eastward propagation of alternating positive and negative OLR anomalies is characteristic of the MJO [e.g., *Madden and Julian*, 1994]. The duration of MJO events is around 32 days (e.g., based on peaks in positive OLR over the Indian Ocean at lags -16 and $+16$ days in Figure 1), which is shorter than the typically cited 40 to 50 day MJO period. However, note that the time separation of individual events based on the OLR-90E index is 40 days (not shown). We explored numerous definitions of the MJO that were based on convection, winds, precipitation, and a combination of these, and found that the qualitative results of the study were consistent independent of which index was used. For example, Figure 1 resembles OLR composites made based on the commonly used MJO index developed by *Wheeler and Hendon* [2004]. The *Wheeler and Hendon* [2004] index determines the phase of a given event based on the relative magnitudes of two principal components calculated from OLR and winds throughout the tropics, whereas the OLR-90E index uses lags based on a convective peak at a single location. This means that while both indices generally identify the same events (e.g., for the 2000–2012 November-April period, there were 47 events identified using the OLR-90 index and 45 using the *Wheeler and Hendon* [2004] index), the OLR-90E index identifies the precise date at which convective forcing is locally strongest, and allows us to most effectively characterize the local impacts of that forcing on the upper ocean.

For the mooring- and satellite-derived variables, which are sampled uniformly in time, we estimated the composite MJO signal at each lag by averaging all of the subseasonal anomalies made within $\pm$1 day of the

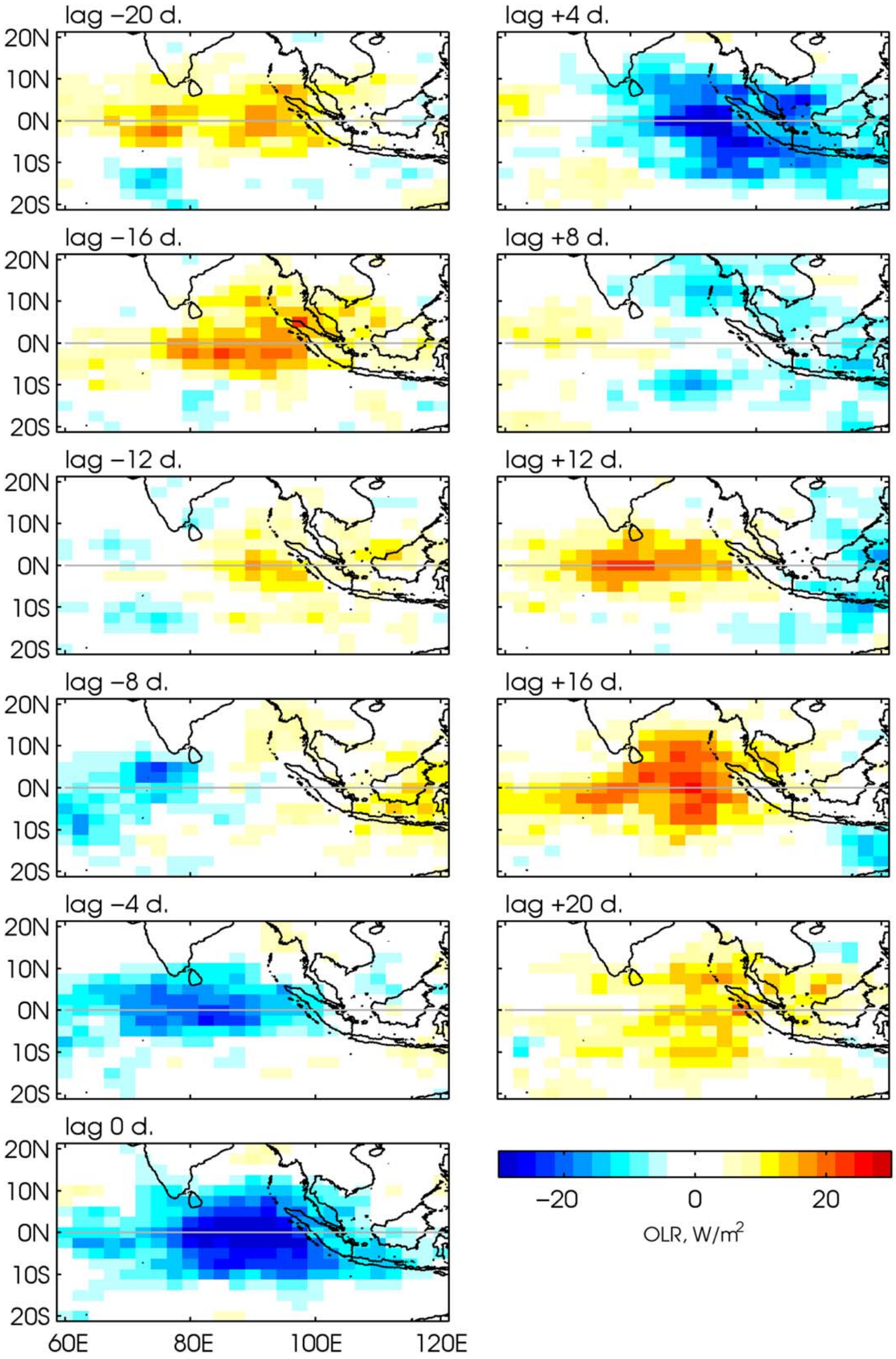

Figure 1. Composite averages of November-April subseasonal OLR. Composites were computed using the OLR-90E index, which was based on intraseasonally band-passed OLR anomalies: (bottom left) lag zero corresponds to dates with a local maxima of negative OLR at 90°E, 0°N, and all other lags from −20 to +20 days computed relative to lag zero.

dates corresponding to that lag. Compositing the Argo data was more complicated, as the profiles are not regularly distributed in time or in space so there are not necessarily enough data points at any given lag to provide a statistically significant average. Instead, we followed the procedure described in detail by *Drushka et al.* [2012] and briefly described here. For each lag $l = -20$ to $+20$ days, we identified all dates that were l days from an MJO peak and collected all Argo profiles made within ±8 days of those dates. For each variable X', where X' represents the anomalous MLD, ILD, or temperature or salinity at one depth, this yielded a set of datapoints at each lag, which we fit to a function using a robust linear least squares regression technique:

$$X'(l)=X_o(l)+\alpha_1(l)t'+\alpha_2(l)t'2+\beta(l)x'+\gamma(l)y', \qquad (2)$$

where t' represents the time difference between each Argo profile and the date of the lag, and x' and y' give the distance from each profile to the mooring site. The regression technique allowed us to exploit the scatter of Argo profiles in order to extract information about MJO-related temporal and spatial signals: the fit yielded $X_o(l)$, the composite average anomaly of X at lag l; $\alpha_1(l)$ and $\alpha_2(l)$, the temporal tendency; and $\beta(l)$ and $\gamma(l)$, the MJO-related longitudinal and latitudinal gradients of X' over the grid box. We also explored including 24 h harmonics in the fit to account for diurnal variations, using the method described by *Gille* [2012] to extract accurate time-of-day information for the Argo profiles, but this did not improve the fits so we excluded this step for simplicity. The standard error on the fit provided an estimate of the uncertainty on each term at each lag. We extended this analysis to the entire domain, computing composite averages at each lag for the data within overlapping 10° longitude × 6° latitude gridboxes.

4. Observations

4.1. Subseasonal Barrier-Layer Variations in the Indian Ocean

Figure 2 illustrates the magnitude of all subseasonal variations in the eastern tropical Indian Ocean during boreal winter. Energetic BLT variations (standard deviation >20 m) are generally coincident with thick (>30 m) mean barrier layers, primarily in the northern Bay of Bengal and in the EEIO (Figure 2a). This is largely because the thickness of a barrier layer can only vary when there is a barrier layer to start with. In the EEIO, the strongest subseasonal BLT variations (standard deviation ~20 m) occur within a few degrees latitude of the equator and extend westward ~15° from Sumatra. Slightly weaker subseasonal BLT variations extend southeastward, hugging the Sumatra coast and tapering off by the time they reach Java. The subseasonal BLT signal in the EEIO coincides with energetic variations in both MLD and ILD, with similar spatial patterns of MLD and ILD (Figures 2c and 2d).

Energetic subseasonal BLT anomalies are also seen in the northern Bay of Bengal, where the mean barrier layer is thick (Figure 2a) due to strong precipitation and runoff [e.g., *Rao and Sivakumar*, 2003]. Subseasonal MLD variability in the Bay of Bengal is weak (Figure 2c), and BLT anomalies appear to arise from ILD variations (Figure 2d). This was also shown by *Girishkumar et al.* [2011], who found that Rossby waves, reflected from intraseasonal Kelvin waves, are responsible for the ILD variations that produce intraseasonal BLT anomalies in the Bay of Bengal. Interestingly, spatial patterns of subseasonal surface salinity variability (Figure 2b) do not resemble those of MLD (Figure 2c). This suggests that although salinity may control the mean MLD in the EEIO and the Bay of Bengal, subseasonal variations in MLD are driven by other processes (e.g., heat fluxes, winds, planetary waves).

Figure 2 simply shows the standard deviation of the subseasonal anomalies, and so represents energy from the MJO, monsoon activity, the quasi-biweekly oscillation, mesoscale eddies, synoptic features, and diurnal variations. To estimate how much of that subseasonal variability is generated by the MJO alone, we used the procedure described in section 3.3 to calculate the MJO composite average for each variable at each time lag and in each gridbox. At each gridpoint, the peak-to-peak amplitude of the MJO-related signal was then estimated as the difference between the maximum and minimum composite values. By comparing Figures 2 and 3, we can infer where the subseasonal variability is likely dominated by the MJO and where other processes are important. In the Bay of Bengal, the strongest subseasonal variations (Figure 2) do not generally correspond to a strong MJO signal (Figure 3). This is unsurprising, since the MJO is largely

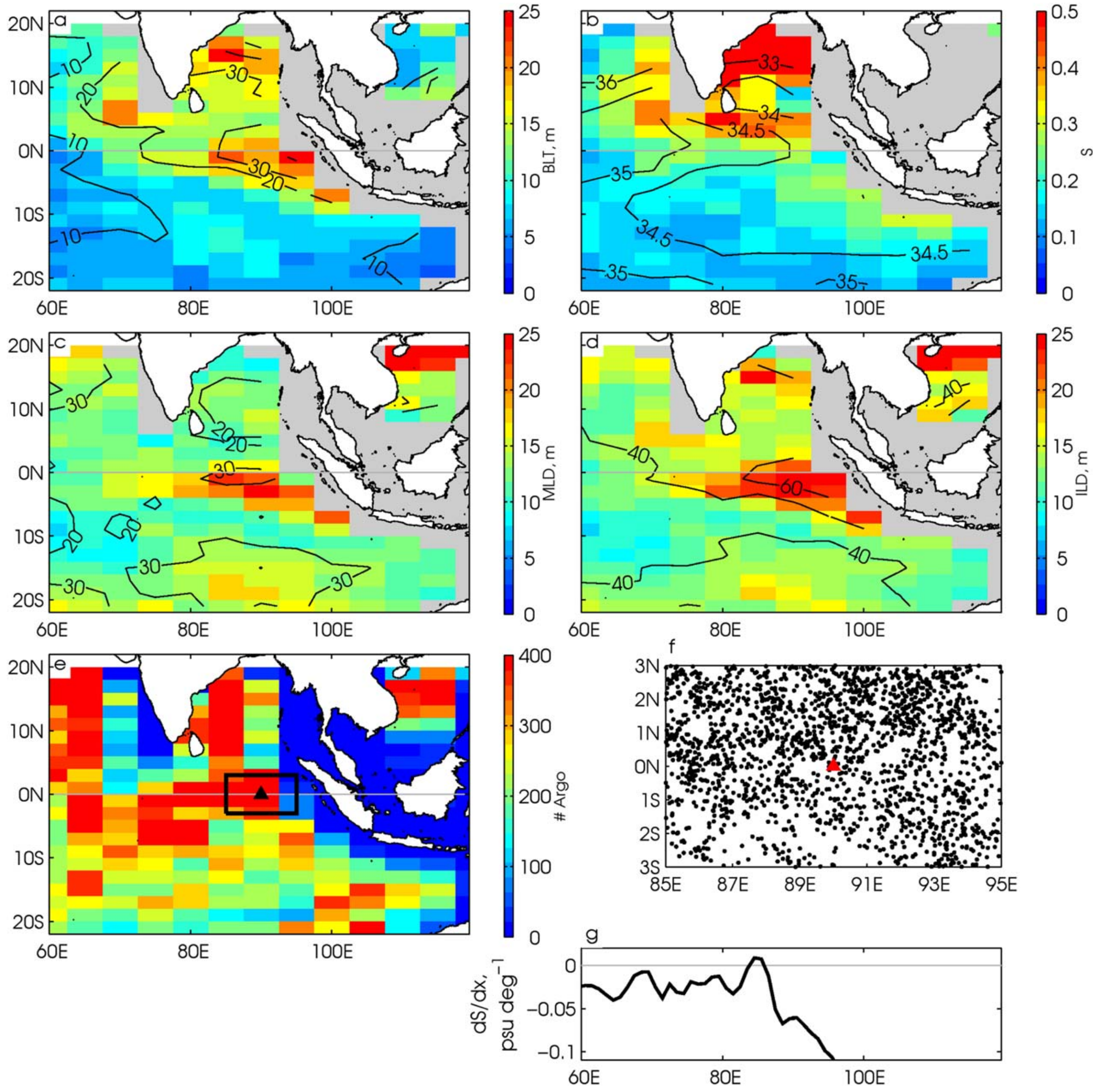

Figure 2. November-April subseasonal variability (colors) and mean (contours) based on Argo: (a) BLT, m; (b) 5 m depth salinity, psu; (c) MLD, m; and (d) ILD, m. For each variable, Argo data in overlapping 10° longitude × 6° latitude gridboxes were collected; the mean was calculated from the unfiltered data and the standard deviation was calculated from the subseasonal anomalies. Gridboxes containing fewer than 50 profiles have been masked out. (e) The number of Argo profiles made during November-April in each gridbox; the triangle indicates the mooring site at 90°E, 0°N, and the black box indicates the region for which Argo profiles were selected to further characterize variability at the mooring site. (f) The spatial distribution of the 1858 Argo profiles within this local mooring region, with the mooring shown as a red triangle. (g) November-April climatological mean zonal salinity gradient along the equator, from Argo data.

confined to the equatorial band and does not exert strong direct impacts in the Bay of Bengal [e.g., *Wheeler and Hendon*, 2004]. In contrast, MJO patterns of MLD and ILD in the EEIO (Figures 3c and 3d) bear a striking resemblance to the subseasonal MLD and ILD variations (Figures 2c and 2d), suggesting that the MJO drives systematic MLD and ILD anomalies in the EEIO. Similarly, the subseasonal salinity variations in the EEIO (Figure 2b), which are weaker than those in the Bay of Bengal but nonzero and extend down the Sumatra coast toward Java, also resemble the MJO composite salinity signal (Figure 3b). However, despite significant MJO signals in composite MLD and ILD, the composite BLT signal in the EEIO is weak (<6 m), and elsewhere in the study region the signal is negligible (Figure 3a). In other words, although subseasonal BLT variations are energetic in the EEIO, the MJO does not appear to force systematic anomalies in BLT.

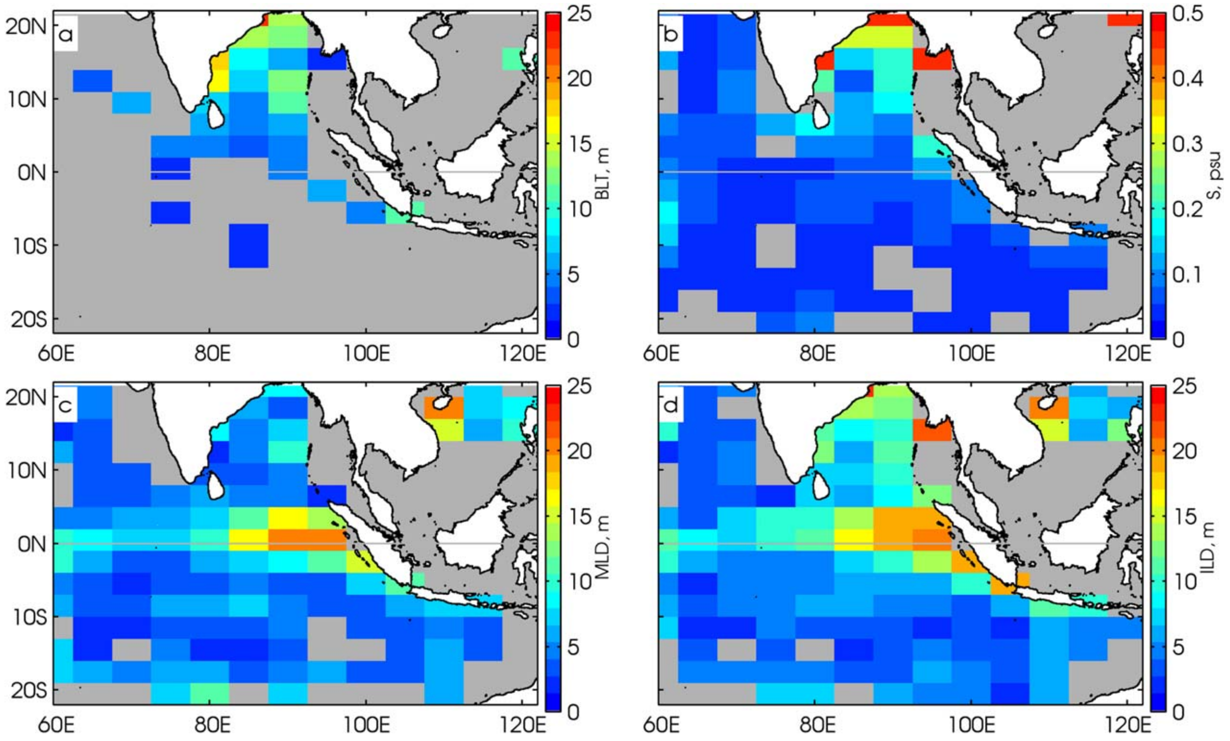

Figure 3. Peak-to-peak amplitude of composite MJO anomalies of (a) BLT, m; (b) 5 m depth salinity, psu; (c) MLD, m; (d) ILD, m. Data are for the November-April period. For each variable, Argo data in overlapping 10° longitude × 6° latitude gridboxes were collected, and composited according to the procedure described in section 3.3. Gridboxes where the composite averages were smaller than their estimated uncertainties, and those containing fewer than 150 profiles, were masked out in gray.

4.2. MJO Variations in the Eastern Equatorial Indian Ocean

To better understand why the MJO-composite BLT signal is weak in the EEIO (Figure 3a) despite strong subseasonal BLT variations there (Figure 2a), we examine the subsurface variations at the site of a RAMA mooring at 90°E,0°N. Figure 4 shows two examples of observations made at this mooring site during MJO events in December 2007 and February 2011. Qualitatively, the atmospheric forcing appears similar for the two events: negative OLR (Figures 4a and 4g), wind stress (Figures 4b and 4h) and precipitation (Figures 4c and 4i) were all maximum within ±1 day of the event "peaks" (i.e., lag zero of the MJO index) on 24 December 2007 and 2 February 2011. However, the upper ocean response to the two cases was substantially different. During the 2007 event, OLR began to decrease around a week before the peak (Figure 4a) and the wind picked up 2 days before the peak (Figure 4b). These cloudy and windy MJO conditions cooled the surface, and due to the relatively weak vertical temperature stratification in the top 80 m, the isothermal layer rapidly thickened (Figure 4d). Meanwhile, freshening in the mixed layer until 1 day before the peak (Figure 4e) kept the mixed-layer stratification stable (Figure 4f) and so the MLD remained shallow until 23 December. As a result, the barrier layer thickened as the event ramped up, producing a large (80 m) BLT anomaly 1 day before the MJO peak.

In contrast, strong negative OLR anomalies began only 2 days before the 2011 event (Figure 4g), and a moderately strong vertical temperature gradient at around 35 m depth prevented the isothermal layer from rapid thickening, so ILD deepened only weakly in the days before the MJO peak on 2 February (Figure 4j). Despite negligible rainfall before the peak (Figure 4j), the upper ocean freshened around a week before the peak (Figure 4k), keeping the upper ocean stable throughout the MJO forcing period (Figure 4l). By 2 February, the vertical temperature gradient at the base of the isothermal layer had weakened enough that the strong wind and convection at the MJO peak was sufficient to rapidly deepen the ILD; as a result, the barrier layer thickened by tens of meters 1 day after the peak.

Figure 4 demonstrates that subtle variations in the relative strength and timing of the convection, wind, and precipitation anomalies associated with individual MJO events, combined with differences in the underlying ocean stratification, can force substantially different changes in the response of the upper ocean. As

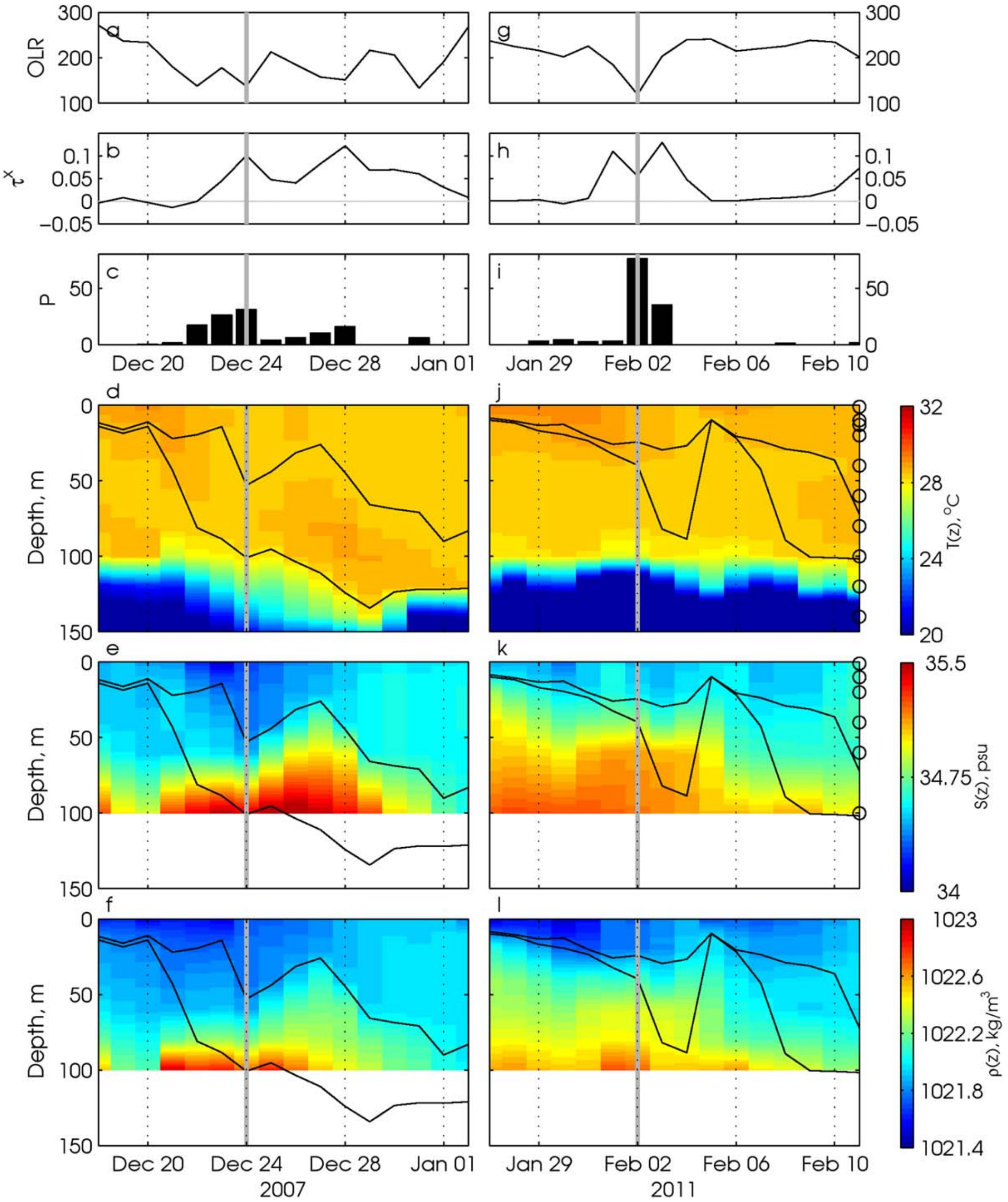

Figure 4. Example of two MJO events observed at the 90°E mooring during (left) 2007 and (right) 2011. (a and g) OLR, W m^{-2}; (b and h) zonal wind stress, N m^{-2}; (c and i) daily precipitation, mm d^{-1}; (d and j) temperature from the RAMA mooring, °C; (e and k) salinity from the RAMA mooring, psu; (f and l) density, computed from the temperature and salinity data, kg m^{-3}. Data from all fields are unfiltered. The lag-zero date of the MJO events are indicated on each plot with a vertical gray line. Circles on the right-hand side of plots 4j and 4k indicate depths of the mooring temperature and salinity sensors, respectively. The black lines on plots 4d–4f and 4j–4l indicate MLD and ILD estimated from the mooring time series. Note that salinity data only go down to 100 m.

described in section 3.1, Figure 4 also illustrates that although the vertical resolution of the mooring data is adequate for resolving the general characteristics of temperature and salinity variations, the salinity sensors in the top 50 m, where most of the MLD variations are seen, are spaced 10–20 m apart (Figure 4k), and the vertical spacing of temperature sensors around the base of the isothermal layer is 20 m (Figure 4j). As a

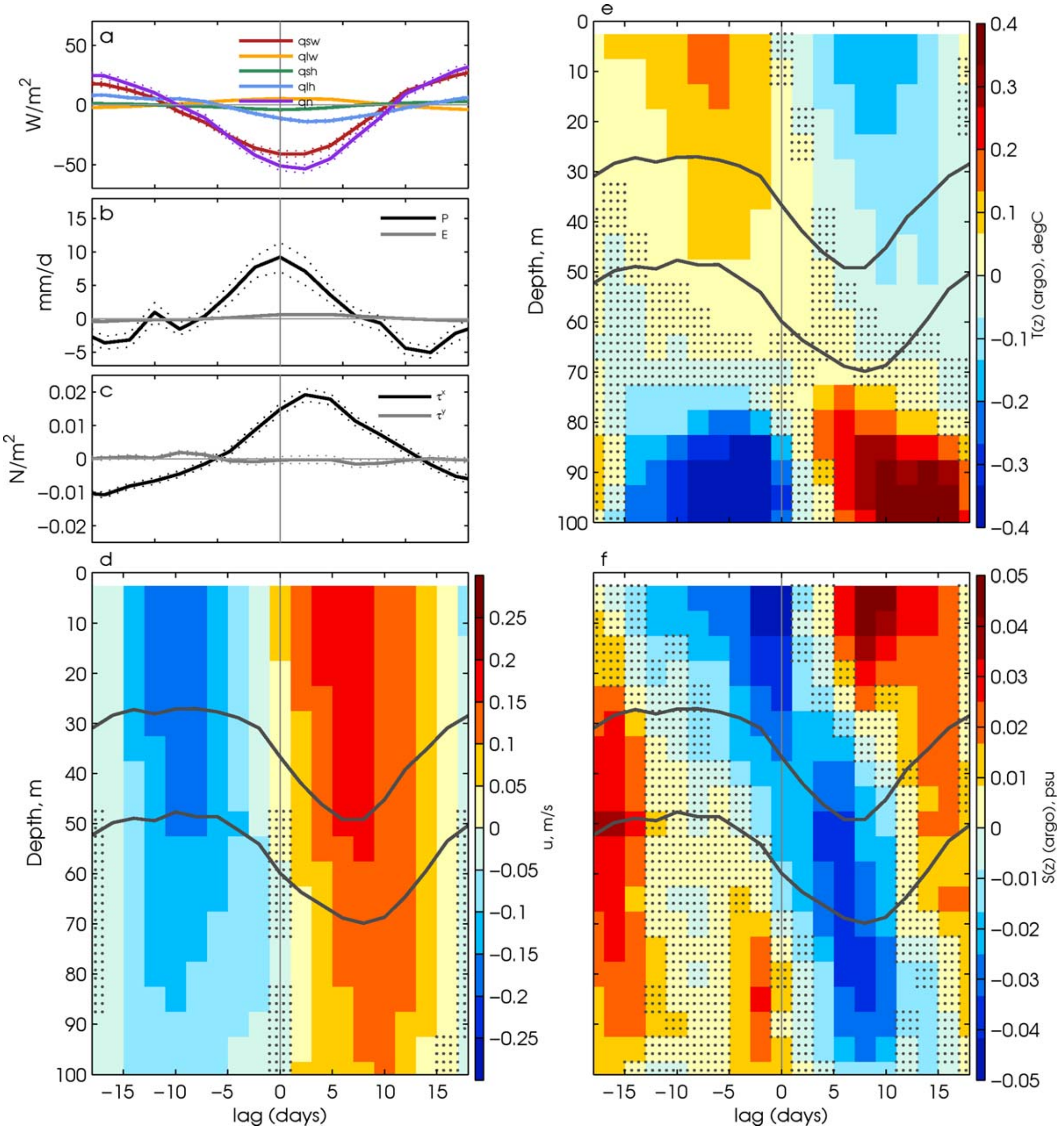

Figure 5. MJO composites near the 90°E, 0°N mooring site. Composites were made using subseasonal anomalies of November-April data and were based on the OLR-90E index. (a) Heat flux components, W m^{-2} (red: shortwave, yellow: longwave, green: sensible, blue: latent) and net heat flux (purple), with positive values indicating heat flux into the upper ocean; (b) precipitation (black) and evaporation (gray), mm d^{-1}; (c) zonal (black) and meridional (gray) wind stress, N m^{-2}; (d) zonal velocity, from the RAMA mooring, m s^{-1}; (e and f) temperature and salinity profiles from Argo, in °C and psu, respectively. In plots 5a–5c, dotted lines indicate the standard error on each average; for plots 5d–5f, the stippling indicates where the composite average is smaller than the standard error and the dark gray lines indicate the composite MLD and ILD. Composites to the Argo data were based on 47 MJO events and use an average of 589 profiles, located in a 10° longitude × 6° latitude gridbox centered on the mooring, per phase. (Note that a given profile can be used in the composite for more than one phase.)

result, MLD and ILD estimates were coarse, which motivated using Argo data to quantify MLD, ILD, temperature and salinity at the mooring site for the remainder of the study.

Boreal winter MJO-composite atmospheric forcing and ocean response at 90°E, 0°N are shown in Figure 5. Net heat flux into the ocean, which is caused almost entirely by shortwave radiation anomalies, peaks at lag zero (Figure 5a); this reflects that the MJO index is based on OLR, which is a proxy for convection, and convection controls the shortwave radiation anomalies. From lags −8 to +8 days, heat flux is negative, indicating the active phase of the MJO; at lags <–8 days and >+8 days, heat flux anomalies are positive (Figure 5a). Precipitation anomalies are in phase with convection and also peak at lag zero; evaporation, which arises from wind anomalies, is negligible (Figure 5b). The uncertainty in precipitation is large compared to uncertainties in other terms: this is likely because rainfall is sporadic and spatially patchy, and varies widely from one event to the next, and also perhaps that satellite-derived estimates of precipitation may be noisy. Zonal wind stress lags convection slightly, peaking at a lag of +2 days, whereas meridional wind stress is effectively zero (Figure 5c). The MJO-composite zonal current response, estimated from the RAMA mooring, reveals that velocity anomalies lag wind stress by around 6 days, with a westward peak of -0.15 m s^{-1} at lag -10 days and an eastward peak of $+0.2$ m s^{-1} at lag +7 days (Figure 5d). The velocity signal penetrates to below the base of the isothermal layer. The deep signal lags the surface slightly, suggesting downward phase propagation with a slope (dz/dt) of around 100 m over 4 days; though the surface signal is stronger than that at depth, the signals appear obviously coherent. This phasing is consistent with a time series of intraseasonal velocities from this mooring site shown by *Masumoto et al*. [2005].

Composite Argo temperatures (Figure 5e) also show variability throughout the top 100 m, but the anomalies within the mixed layer appear to be distinct from those below the isothermal layer, illustrating that the barrier layer can indeed decouple the surface from the thermocline. Mixed-layer temperature lags heat flux (Figure 5a) by about one-quarter cycle, with the peak cold anomaly at a lag of +8 days: this is consistent with previous studies [e.g., *Drushka et al*., 2012] showing that anomalous heat fluxes drive MJO-related SST anomalies.

The peak-to-peak surface salinity anomaly induced by the MJO at 90°E, 0°N, though small (±0.1 psu) compared to the MJO salinity anomaly in the Bay of Bengal (Figure 3b), is statistically significant, and is consistent with previous estimates [*Matthews et al*., 2010; *Grunseich et al*., 2011, 2013]. Mixed-layer freshening begins at around lag -13 days, producing a maximum negative salinity anomaly of -0.05 psu at lag -2 days (Figure 5f), that is, prior to the precipitation anomaly, which peaks at lag zero (Figure 5b). This indicates that the freshening is driven by a process other than rainfall, as seen in the MJO events shown in Figure 4. Although uncertainties are too large to estimate a complete mixed-layer salinity budget, the phasing and magnitude of zonal salinity advection can be estimated based on the mean zonal salinity gradient at 90°E, 0°N (around -0.07 psu (degree longitude)$^{-1}$; Figure 2g) and the composite zonal surface velocity anomaly, which averages -0.1 m s^{-1} from lag -12 to -7 days (Figure 5d). This anomalous current acting on the mean salinity gradient would produce local freshening at a rate of around 0.006 psu d^{-1}, yielding a 0.04 psu decrease from lag -12 to -5 days, which is roughly consistent with what is observed (Figure 5f). During lags 0 to +10 days, eastward velocity anomalies (Figure 5d) bring in saltier water from the west, resulting in surface salinification (Figure 5f) despite the local precipitation (Figure 5b). The advection-driven fresh anomaly during negative lags produces a fresh, stable mixed layer upon which the MJO acts.

During active MJO conditions (lags -8 to +8 days), winds and surface cooling both help to deepen the mixed layer and the isothermal layer by ~20 m. However, since MLD and ILD vary in tandem, the thickness of the barrier layer between them does not change during the course of the MJO cycle (Figures 5d–5f). This explains why the peak-to-peak BLT anomalies throughout the domain are small (Figure 3a), even in regions where MLD and ILD anomalies are large (Figures 3c and 3d).

In addition to the signals within the mixed layer, there are significant composite MJO anomalies in both temperature and salinity below ~80 m. The deep MJO temperature anomaly is particularly striking, with a peak-to-peak amplitude of 1°C (Figure 5e). This corresponds to the depth of the thermocline, where the vertical temperature gradient is strong, and anomalous vertical velocities (w') forced by the MJO can produce vertical heat advection. Temperature at 100 m increases during lags -5 to +10 days, indicating downward advection of warmer water from above. Indeed, if the sign of w' is inferred from the derivative of ILD, w' is negative (isothermal-layer deepening) during lags -6 to +8 days, roughly consistent with this phasing. Though the deep salinity signal is noisier than that of temperature, freshening at 90 m depth is seen during lags 0 to +8 days (Figure 5f), which can be at least somewhat attributed to downward velocity advecting freshwater from above.

4.3. Impacts of an Existing Barrier Layer

So far, we have only considered the impacts of the MJO on the barrier layer. Now, we examine whether the presence of a barrier layer affects the SST response to MJO forcing. It is generally hypothesized that when a barrier layer is present, atmospheric forcing is trapped within a thinner and more strongly stratified mixed layer, so incoming fluxes of heat, freshwater and momentum will produce relatively strong anomalies in

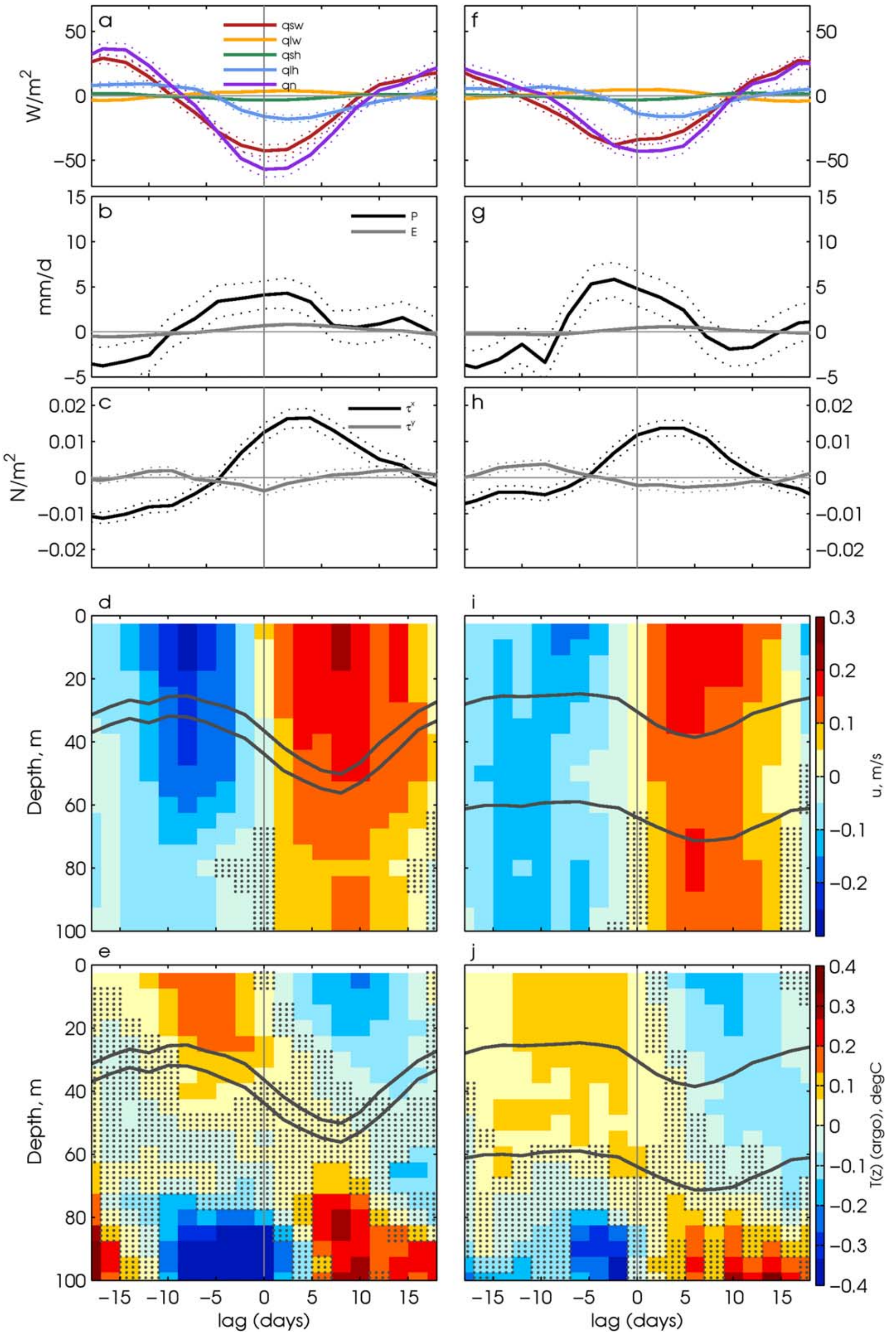

Figure 6. Similar to Figures 5a–5e, except that composites were based only on profiles for which (a–e) BLT was thinner than 10 m, and (f–j) BLT at lag zero was thicker than 10 m. (Figures 6a and 6f) Heat flux components, W m^{-2}; (Figures 6b and 6g) precipitation (black) and evaporation (gray), mm d^{-1}; (Figures 6c and 6h) zonal (black) and meridional (gray) wind stress, N m^{-2}; (Figures 6d and 6i) zonal velocity, from the RAMA mooring, m s^{-1}; (Figures 6e and 6j) temperature profiles from Argo, °C. Argo composites of thin-barrier layer cases used an average of 276 profiles per phase; those for thick-barrier layer cases used an average of 313 profiles per phase. The two cases are defined based on the BLT of each profile and not by the MJO events, so both thick-BLT and thin-BLT cases were based on 47 MJO events.

temperature, salinity and velocity. On the other hand, a barrier layer reduces the temperature gradient at the base of the mixed layer, and thus the entrainment cooling that occurs when the mixed layer deepens; this could produce weaker anomalies in SST. We assess these hypotheses by separating Argo profiles for which the local barrier layer is thin (<10 m) and thick (>10 m), and computing separate composites for the two cases. The goal here is to assess whether the presence or absence of a barrier layer has an impact on MJO forcing—regardless of what caused the barrier layer to be thick or thin in the first place—so we separate profiles based on their unfiltered BLT only. We also subsample the atmospheric forcing terms to the times of each Argo profile and composite them separately for the thin-barrier layer and thick-barrier layer cases in order to quantify how much of the difference in ocean response is due to atmospheric forcing.

The most striking difference between the two cases is the amplitude of the MLD and ILD anomalies forced by the MJO. In the thin-barrier layer case, excursions in both MLD and ILD exceed ±12 m (Figures 6d and 6e), compared to only ±5 m for the thick-barrier layer case (Figures 6i and 6j). The atmospheric forcing is fairly similar for the two cases, with ~15% stronger heat flux and wind stress for the thick-barrier layer composites, and ~10% stronger precipitation for the thin-barrier layer cases (Figures 6a–6c and 6f–6h). Although the stronger winds for the thin-barrier layer case would tend to deepen the mixed layer more, this alone cannot account for the much stronger deepening of the MLD and ILD. Evidently, the strong mixed-layer stratification that produces a thick barrier layer also reduces the ability of MJO wind and buoyancy forcing to deepen the mixed layer and the isothermal layer.

The MJO-composite mixed-layer temperature anomaly is much greater for the thin-barrier layer case than for the thick-barrier layer case, with a magnitude of ±0.2°C compared to ±0.1°C (Figures 6e and 6j). Only around 15% of this discrepancy can be explained by the stronger heat flux forcing in the thin-barrier layer case (Figures 6a and 6f); the remainder must be due to differences in vertical entrainment. A thick barrier layer reduces vertical excursions in MLD as well as the temperature gradient at the base of the mixed layer; both of these factors reduce entrainment cooling in the thick-barrier layer case (Figure 6j). In contrast, when the barrier layer is absent the water temperature jump at the base of the mixed layer is much larger. Combined with the larger MJO-forced swings in MLD (which are due to weaker stratification and stronger winds, as discussed just above), this produces particularly strong entrainment, and hence the strong temperature anomalies, in the thin-barrier layer case (Figure 6e).

5. Discussion

5.1. MJO Versus Subseasonal Barrier-Layer Variations

Figure 2a shows that subseasonal BLT variability in the EEIO is strong, but it remains unclear what generates this variability. Although the composite MJO BLT signal is negligible (Figure 5), Figures 4g–4l show the barrier layer thickening by nearly 50 m during an MJO event. There are two likely causes of this discrepancy: the diversity of individual MJO events, and subseasonal variations not related to the MJO.

The composites reveal that anomalous winds, convection, and rainfall associated with the MJO drive systematic changes in momentum, temperature, and salinity, all of which can generate anomalies in MLD and ILD on time scales of a few days (Figure 5). However, even subtle differences in the background stratification or the relative phasing of MJO precipitation and wind anomalies can produce significant differences in the response of the upper ocean. This can be seen by comparing the two events shown in Figure 4. If mixed-layer freshening preceding the MJO is strong, the MLD remains shallow despite MJO wind forcing (Figures 4g–4l). If the background temperature stratification is weak, the isothermal-layer deepening may occur rapidly, producing a BLT anomaly at the onset of MJO conditions (Figures 4a–4f). On the other hand, if the freshening is weak or if the MJO wind anomalies occur a day or two early, the mixed layer may deepen quickly, eliminating the barrier layer completely. When these disparate events are averaged, the result is a negligible composite anomaly despite potentially large BLT variations during individual MJO events. This is consistent with the model study of *Schiller and Godfrey* [2003], which showed that the variance across individual events exceeds the composite average. This may also explain why BLT composite anomalies are negligible despite the significant salinity upper ocean anomalies (Figure 5f), which might be expected to drive changes in the barrier layer: while salinity can affect BLT by modulating MLD, the relative strength of salinity and wind variations varies from event to event, so the composite BLT does not appear correlated with composite salinity.

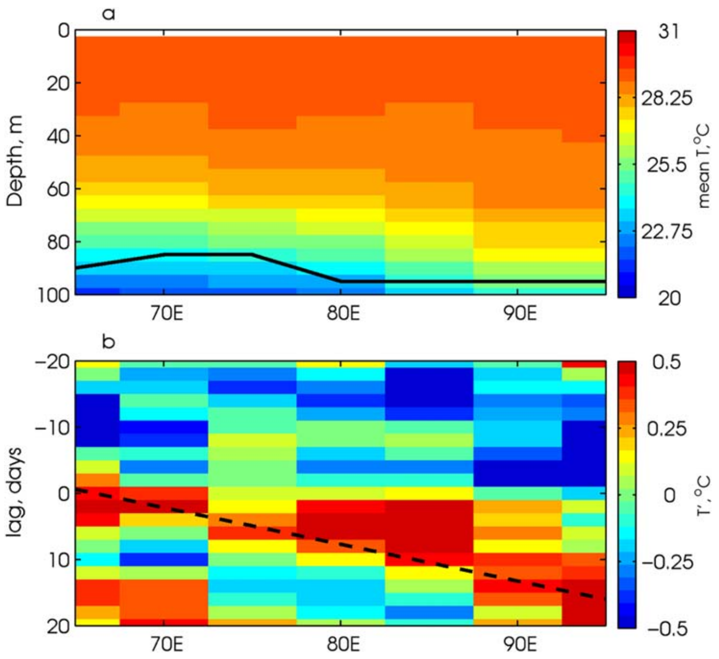

Figure 7. (a) November-April mean temperature in the top 100 m along the equator in the central and eastern Indian Ocean, computed from Argo profiles in overlapping 10° longitude × 6° latitude gridboxes. The depth of the thermocline, estimated as the strongest vertical temperature gradient at each longitude, is shown as a thick black line. (b) MJO-composite temperature anomaly at the depth of the thermocline, shown at each time-lag and at each longitude along the equator. The dashed black line indicates the eastward propagation of the strongest positive temperature anomalies at the thermocline depth.

Subseasonal variations in the barrier layer that are not associated with the MJO are also likely energetic, and hence contribute to the discrepancy between subseasonal and MJO-composite BLT anomalies in Figures 2a and 3a. Winds and rainfall in this region are spatially and temporally intermittent, even within the envelope of MJO events [*Chen et al*., 1996], and one can imagine any number of scenarios that would result in significant changes in the thickness of the barrier layer on time scales of a few days or less. For example, moderate winds could deepen the mixed layer without changing the vertical temperature structure of the water column, causing the barrier layer to collapse. A clear and windless afternoon could produce a thin surface warm layer, causing both the MLD and ILD to shoal rapidly, again collapsing the barrier layer (e.g. February 5 in Figure 4). A very strong local rain squall not accompanied by winds could produce a surface fresh lens and a thin mixed layer without altering the ILD, leading to a thick barrier layer. Unraveling the dynamics driving high-frequency variations in BLT is not possible in the present study: BLT estimates from the moorings are not accurate enough, and the Argo data are too irregular in time. We thus conclude that both the MJO and other subseasonal variations drive anomalies in the thickness of the barrier layer.

5.2. Deep Vertical Motions

The large composite temperature and salinity anomalies in the thermocline (Figures 5e and 5f) likely arise from vertical advection, which invites the question of what causes the vertical velocity anomalies (w') at the thermocline depth. The vertical velocity can be roughly inferred from the rate of change in the ILD, which is negative (deepening) during active MJO conditions (lags −6 to +6 days) and has a maximum value of around 1 m d^{-1} at lag zero (Figures 5d–5f). There are a few possible causes of this downward vertical velocity. First, the timing is consistent with being driven by turbulent mixing from winds, which are anomalously westerly during lags −5 to +10 days (Figure 5c) and could cause turbulent mixing down to the thermocline depth. Westerly wind anomalies on the equator also produce Ekman convergence and thus downwelling [*Lukas and Lindstrom*, 1991]; again, the timing is consistent with this mechanism. Finally, intraseasonal westerly wind anomalies can excite downwelling Kelvin waves that propagate eastward along the equator, producing negative vertical velocity anomalies. The temperature signature of Kelvin waves is largest where the vertical temperature gradient is strong, i.e. at the thermocline. To assess whether the observed thermocline temperature anomaly seen at the 90°E mooring site could be related to Kelvin waves, we computed MJO composites in the gridboxes along the equator throughout the domain, and extracted the composite temperature anomaly at the thermocline depth (Figure 7a). Thermocline temperature anomalies of ±0.5°C are seen throughout the domain, from longitudes 65°E to 95°E (Figure 7b). The eastward propagation speed, estimated by fitting a line to the strongest positive temperature anomalies, is around 2 m s^{-1}, consistent with the propagation speed of Kelvin waves across the Indian Ocean [*Drushka et al*., 2010] and much slower

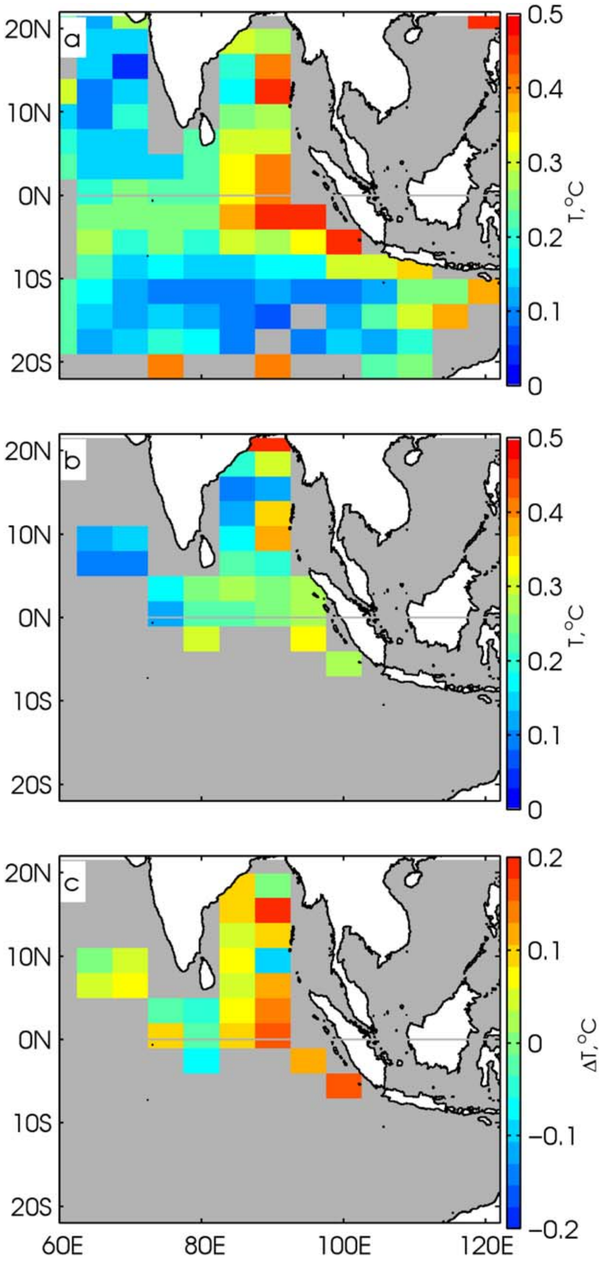

Figure 8. Peak-to-peak MJO-composite 5 m temperature anomalies, where composites are based on November-April Argo profiles from 2000 to 2012, and only data with lag-zero barrier layers that are (a) thinner than 10 m and (b) thicker than 10 m are used. (c) The temperature difference between the thick and thin cases (a minus b). Gridboxes where the composite averages were smaller than their estimated uncertainties, and those containing fewer than 20 profiles, were masked out in gray.

than the ∼5 m s^{-1} propagation speed of the MJO [*Zhang*, 2005]. This is compelling evidence that the strong composite temperature anomalies below 80 m (Figure 5e) could be caused by vertical velocities associated with wind-driven Kelvin waves.

We are unable to determine which mechanism—equatorial convergence, wind mixing, or Kelvin waves—is the main driver of vertical velocity anomalies, and hence large temperature and salinity anomalies, below ∼80 m depth on MJO time scales. However, MLD and ILD anomalies related to the MJO are largely confined to the equatorial band (Figures 2c and 2d), hinting that equatorial convergence and Kelvin wave forcing may be the dominant processes.

5.3. Potential Feedback Mechanisms

Figure 6 shows that the presence or absence of a barrier layer at the 90°E, 0°N mooring site can significantly affect the SST anomalies that are excited by the MJO. We estimate the magnitude of this effect throughout the study domain by computing the peak-to-peak mixed-layer temperature signal (c.f. Figure 3) for both thin-barrier and thick-barrier layer cases. In the EEIO, the MJO forces SST anomalies with an amplitude exceeding 0.4°C when the barrier layer is thin (Figure 8a). In contrast, when the barrier layer is thick, MJO-related SST anomalies in the EEIO are less than 0.2°C (Figure 8b). Similarly, SST anomalies in the Bay of Bengal associated with the MJO are weaker for the thick-barrier layer case. Indeed, throughout the region east of 80°E and north of 10°S, the MJO excites peak-to-peak SST anomalies that are 0.1–0.25°C stronger if the barrier layer is thin compared to if the barrier layer is thick (Figure 8c). Though the degree to which air-sea coupling is important for the MJO is contentious [*Zhang*, 2005], atmosphere-only models forced by intraseasonal SSTs can simulate the MJO [e.g., *Woolnough et al.*, 2001]. This suggests that the magnitude of the SST anomalies excited by the MJO can affect local atmospheric dynamics, and hence can feed back onto the ocean. By modulating MJO-related SSTs, anomalies in BLT could thus have significant consequences for feedbacks related to the MJO in the Indian Ocean. This provides a mechanism by which low-frequency (seasonal, interannual) anomalies in ocean stratification can influence MJO-scale SST anomalies.

6. Summary

Ocean observations from Argo profiling floats reveal energetic (standard deviation >20 m) subseasonal variations in boreal winter BLT in the EEIO and the Bay of Bengal (Figure 2). In the Bay of Bengal, subseasonal surface salinity variations are also strong, though they do not appear to drive MLD variations, and subseasonal BLT variations instead appear related to anomalies in the ILD. In the EEIO, subseasonal BLT variability is linked to variations in both MLD and ILD. The subseasonal band encompasses a range of processes, including intraseasonal (dominated by the MJO), monsoon active/break activity, quasi-biweekly oscillations, diurnal variations, and mesoscale and synoptic features. To assess how much of the subsurface signal results from the MJO, composites were formed based on an index of intraseasonal OLR at 90°E, 0°N. The composites reveal that the Bay of Bengal sees no significant MJO-related variations in MLD, ILD or the barrier layer (Figure 3). In the EEIO, strong MJO-related anomalies in MLD and BLT are seen within a few degrees north and south of the equator and stretching west of Sumatra to around 90°E. Interestingly, although BLT is calculated as the difference between ILD and MLD, MJO composite anomalies of BLT in the EEIO are weak (<5 m peak-to-peak) or statistically insignificant (Figure 3a). This can be understood by considering composite depth sections at 90°E, 0°N, which reveal that MLD and ILD vary in tandem and so the thickness of the layer between them (i.e., the barrier layer) does not change (Figure 5). We posit that the MJO does, in fact, drive anomalies in BLT, but because individual events are highly variable, the composite average is smoothed out. This helps to explain the discrepancy between subseasonal and MJO-composite BLT variability.

In the composite average of all MJO events, westward surface currents advect fresher water from the Sumatra coast around 5 days before the peak in MJO forcing, producing a relatively stable mixed layer. As a result, the mixed layer of the EEIO responds strongly to MJO atmospheric forcing, with peak-to-peak SST anomalies of around 0.3°C and a sea surface salinity signal of 0.1 psu (Figures 5e and 5f).

The upper ocean temperature response to MJO forcing is significantly reduced when the barrier layer is thick. This is most likely due to modulation of entrainment cooling, which occurs (a) because the thick barrier layer (and slightly weaker wind forcing) reduces mixed-layer deepening during the active MJO; and (b) because when a barrier layer is present, water below the mixed layer is the same temperature as that within the mixed layer, so entrainment of deeper water does not cause cooling. This effect is widespread: throughout the EEIO and the Bay of Bengal, the MJO excites surface temperature anomalies that are over 0.1°C (peak-to-peak) greater if the barrier layer is thin as compared to if it is thick (Figure 8c). Since SST drives convection, this suggests a potential link between the presence or absence of a barrier layer and the feedback of MJO-generated SST anomalies onto the atmosphere.

Acknowledgments
This work was supported by NOAA grant NA10OAR4310139 (STG), NSF grant ARRA OCE0850350 (STG) and NASA award NNX13AO38G (JS). We gratefully acknowledge the primary sources of data for this study: mooring data were provided by the TAO Project Office of NOAA/PMEL. The Argo data were collected and made freely available by the International Argo Program and the national programs that contribute to it. (www.argo.ucsd.edu, argo.jcommops.org); the Argo Program is part of the Global Ocean Observing System. We also wish to thank two anonymous reviewers for their feedback.

References

Agarwal, N., R. Sharma, A. Parekh, S. Basu, A. Sarkar, and V. K. Agarwal (2012), Argo observations of barrier layer in the tropical Indian Ocean, *Adv. Space Res.*, *50*, 642–654.

Anderson, S., R. Weller, and R. Lukas (1996), Surface buoyancy forcing and the mixed layer of the western Pacific warm pool: Observations and 1D model results, *J. Clim.*, *9*(12), 3056–3085.

Annamalai, H., R. Murtugudde, J. Potemra, S. Xie, P. Liu, and B. Wang (2003), Coupled dynamics over the Indian Ocean: Spring initiation of the zonal mode, *Deep Sea Res., Part II*, *50*(12), 2305–2330.

Bosc, C., T. Delcroix, and C. Maes (2009), Barrier layer variability in the western Pacific warm pool from 2000 to 2007, *J. Geophys. Res.*, *114*, C06023, doi:10.1029/2008JC005187.

Chen, S., R. Houze, and B. Mapes (1996), Multiscale variability of deep convection in realation to large-scale circulation in TOGA COARE, *J. Atmos. Sci.*, *53*(10), 1380–1409.

Chowdary, J., C. Gnanaseelan, and S. Xie (2009), Westward propagation of barrier layer formation in the 2006–07 Rossby wave event over the tropical southwest Indian Ocean, *Geophys. Res. Lett.*, *36*, L04607, doi:10.1029/2008GL036642.

Cronin, M., and M. McPhaden (2002), Barrier layer formation during westerly wind bursts, *J. Geophys. Res.*, *107*(C12), 8020, doi:10.1029/2001JC001171.

de Boyer Montégut, C., G. Madec, A. Fischer, A. Lazar, and D. Iudicone (2004), Mixed layer depth over the global ocean: An examination of profile data and a profile-based climatology, *J. Geophys. Res.*, *109*, C12003, doi:10.1029/2004JC002378.

de Boyer Montégut, C., J. Mignot, A. Lazar, and S. Cravatte (2007), Control of salinity on the mixed layer depth in the world ocean: 1. General description, *J. Geophys. Res.*, *112*, C06011, doi:10.1029/2006JC003953.

Drushka, K., J. Sprintall, S. Gille, and I. Brodjonegoro (2010), Vertical structure of Kelvin waves in the Indonesian Throughflow, *J. Phys. Oceanogr.*, *40*(9), 1965–1987, doi:10.1175/2010JPO4380.1.

Drushka, K., J. Sprintall, S. Gille, and S. Wijffels (2012), In situ observations of Madden-Julian Oscillation mixed layer dynamics in the Indian and western Pacific Oceans, *J. Clim.*, *25*(7), 2306–2328.

Duvel, J., R. Roca, and J. Vialard (2004), Ocean mixed layer temperature variations induced by intraseasonal convective perturbations over the Indian Ocean, *J. Atmos. Sci.*, *61*(9), 1004–1023.

Gille, S. (2012), Diurnal variability of upper ocean temperatures from microwave satellite measurements and Argo profiles, *J. Geophys. Res.*, *117*, C11027, doi:10.1029/2012JC007883.

Girishkumar, M., M. Ravichandran, M. McPhaden, and R. Rao (2011), Intraseasonal variability in barrier layer thickness in the south central Bay of Bengal, *J. Geophys. Res.*, *116*, C03009, doi:10.1029/2010JC006657.

Godfrey, J., and E. Lindstrom (1989), The heat budget of the equatorial western Pacific surface mixed layer, *J. Geophys. Res.*, *94*(C6), 8007–8017.

Gottschalck, J., et al. (2010), A framework for assessing operational Madden-Julian oscillation forecasts: A CLIVAR MJO working group project, *Bull. Am. Meteorol. Soc.*, *91*(9), 1247–1258.

Graham, N., and T. Barnett (1987), Sea surface temperature, surface wind divergence, and convection over tropical oceans, *Science*, *238*(4827), 657–659.

Grunseich, G., B. Subrahmanyam, and A. Arguez (2011), Influence of the Madden-Julian Oscillation on sea surface salinity in the Indian Ocean, *Geophys. Res. Lett.*, *38*, L17605, doi:10.1029/2011GL049047.

Grunseich, G., B. Subrahmanyam, and B. Wang (2013), The Madden-Julian oscillation detected in Aquarius salinity observations, *Geophys. Res. Lett.*, *40*, 5461–5466, doi:10.1002/2013GL058173.

Hendon, H. H., B. Liebmann, M. Newman, J. D. Glick, and J. Schemm (2000), Medium-range forecast errors associated with active episodes of the Madden-Julian Oscillation, *Mon. Weather Rev.*, *128*(1), 69–86.

Huffman, G. J., D. T. Bolvin, E. J. Nelkin, D. B. Wolff, R. F. Adler, G. Gu, Y. Hong, K. P. Bowman, and E. F. Stocker (2007), The TRMM Multisatellite Precipitation Analysis (TMPA): Quasi-global, multiyear, combined-sensor precipitation estimates at fine scales, *J. Hydrometeorol.*, *8*(1), 38–55.

Liebmann, B., and C. A. Smith (1996), Description of a complete (interpolated) outgoing longwave radiation dataset, *Bull. Am. Meteorol. Soc.*, *77*, 1275–1277.

Lukas, R., and E. Lindstrom (1991), The mixed layer of the western equatorial Pacific Ocean, *J. Geophys. Res.*, *96*(S01), 3343–3357.

Madden, R., and P. Julian (1994), Observations of the 40–50-day tropical oscillation-A review, *Mon. Weather Rev.*, *122*(5), 814–837.

Masson, S., P. Delecluse, J. Boulanger, and C. Menkes (2002), A model study of the seasonal variability and formation mechanisms of the barrier layer in the eastern equatorial Indian Ocean, *J. Geophys. Res.*, *107*(C12), 8017, doi:10.1029/2001JC000832.

Masson, S., C. Menkes, P. Delecluse, and J.-P. Boulanger (2003), Impacts of salinity on the eastern Indian Ocean during the termination of the fall Wyrtki Jet, *J. Geophys. Res.*, *108*(C3), 3067, doi:10.1029/2001JC000833.

Masson, S., J. Boulanger, C. Menkes, P. Delecluse, and T. Yamagata (2004), Impact of salinity on the 1997 Indian Ocean dipole event in a numerical experiment, *J. Geophys. Res.*, *109*, C02002, doi:10.1029/2003JC001807.

Masumoto, Y., H. Hase, Y. Kuroda, H. Matsuura, and K. Takeuchi (2005), Intraseasonal variability in the upper-layer currents observed in the eastern equatorial Indian Ocean, *Geophys. Res. Lett.*, *32*, L02607, doi:10.1029/2004GL021896.

Matthews, A., P. Singhruck, and K. Heywood (2010), Ocean temperature and salinity components of the Madden-Julian oscillation observed by Argo floats, *Clim. Dyn.*, *35*(7-8), 1149–1168, doi:10.1007/s00382-009-0631-7.

McPhaden, M., G. Meyers, K. Ando, Y. Masumoto, V. Murty, M. Ravichandran, F. Syamsudin, J. Vialard, L. Yu, and W. Yu (2009), RAMA: The Research Moored Array for African-Asian-Australian Monsoon Analysis and Prediction, *Bull. Am. Meteorol. Soc.*, *90*(4), 459–480.

Mignot, J., C. de Boyer Montégut, A. Lazar, and S. Cravatte (2007), Control of salinity on the mixed layer depth in the world ocean: 2. Tropical areas, *J. Geophys. Res.*, *112*, C10010, doi:10.1029/2006JC003954.

Miyama, T., J. P. McCreary Jr., D. Sengupta, and R. Senan (2006), Dynamics of biweekly oscillations in the equatorial Indian Ocean, *J. Phys. Oceanogr.*, *36*(5), 827–846.

Murtugudde, R., and A. Busalacchi (1999), Interannual variability of the dynamics and thermodynamics of the tropical Indian Ocean, *J. Clim.*, *12*(8), 2300–2326.

Praveen Kumar, B., J. Vialard, M. Lengaigne, V. Murty, and M. McPhaden (2012a), Tropflux: air-sea fluxes for the global tropical oceans–description and evaluation, *Clim. Dyn.*, *38*, 1521–1543, doi:10.1007/s00382-011-1115-0.

Praveen Kumar, B., J. Vialard, M. Lengaigne, V. Murty, M. McPhaden, M. Cronin, F. Pinsard, and K. G. Reddy (2012b), Tropflux wind stresses over the tropical oceans: Evaluation and comparison with other products, *Clim. Dyn.*, *1–23*, doi:10.1007/s00382-012-1455-4.

Qiu, Y., W. Cai, L. Li, and X. Guo (2012), Argo profiles variability of barrier layer in the tropical Indian Ocean and its relationship with the Indian Ocean Dipole, *Geophys. Res. Lett.*, *39*, L08605, doi:10.1029/2012GL051441.

Qu, T., and G. Meyers (2005), Seasonal characteristics of circulation in the southeastern tropical Indian Ocean, *J. Phys. Oceanogr.*, *35*(2), 255–267, doi:10.1175/JPO-2682.1.

Rao, R., and R. Sivakumar (2003), Seasonal variability of sea surface salinity and salt budget of the mixed layer of the north Indian Ocean, *J. Geophys. Res.*, *108*(C1), 3009, doi:10.1029/2001JC000907.

Rao, S. A., and T. Yamagata (2004), Abrupt termination of Indian Ocean dipole events in response to intraseasonal disturbances, *Geophys. Res. Lett.*, *31*, L19306, doi:10.1029/2004GL020842.

Roemmich, D., and J. Gilson (2009), The 2004–2008 mean and annual cycle of temperature, salinity, and steric height in the global ocean from the Argo program, *Prog. Oceanogr.*, *82*(2), 81–100.

Sato, K., T. Suga, and K. Hanawa (2006), Barrier layers in the subtropical gyres of the world's oceans, *Geophys. Res. Lett.*, *33*, L08603, doi:10.1029/2005GL025631.

Schiller, A., and J. Godfrey (2003), Indian Ocean intraseasonal variability in an ocean general circulation model, *J. Clim.*, *16*, 21–39.

Shinoda, T., H. Hendon, and J. Glick (1998), Intraseasonal variability of surface fluxes and sea surface temperature in the tropical western Pacific and Indian Oceans, *J. Clim.*, *11*(7), 1685–1702.

Sprintall, J., and M. Tomczak (1992), Evidence of the barrier layer in the surface layer of the tropics, *J. Geophys. Res.*, *97*(C5), 7305–7316.

Vecchi, G. A., and D. Harrison (2002), Monsoon breaks and subseasonal sea surface temperature variability in the Bay of Bengal, *J. Clim.*, *15*(12), 1485–1493.

Vialard, J., and P. Delecluse (1998a), An OGCM Study for the TOGA decade. Part II: Barrier-layer formation and variability, *J. Phys. Oceanogr.*, *28*(6), 1089–1106.

Vialard, J., and P. Delecluse (1998b), An OGCM Study for the TOGA decade. Part I: Role of salinity in the physics of the Western Pacific fresh pool, *J. Phys. Oceanogr.*, *28*(6), 1071–1088.

Webber, B., A. Matthews, and K. Heywood (2010), A dynamical ocean feedback mechanism for the Madden–Julian Oscillation, *Q. J. R. Meteorol. Soc.*, *136*, 740–754.

Webber, B. G., A. J. Matthews, K. J. Heywood, and D. P. Stevens (2012), Ocean Rossby waves as a triggering mechanism for primary Madden–Julian events, *Q. J. R. Meteorol. Soc.*, *138*(663), 514–527.

Webster, P. (2002), JASMINE: The scientific basis, *Bull. Am. Meteorol. Soc.*, *83*, 1603–1630.

Weller, R. A., F. Bradley, and R. Lukas (2004), The interface or air-sea flux component of the TOGA Coupled Ocean-Atmosphere Response Experiment and its impact on subsequent air-sea interaction studies, *J. Atmos. Oceanic Technol.*, *21*(2), 223–257.

Wheeler, M., and H. Hendon (2004), An all-season real-time multivariate MJO index: Development of an index for monitoring and prediction, *Mon. Weather Rev.*, *132*, 1917–1932.

Woolnough, S., J. Slingo, and B. Hoskins (2001), The organization of tropical convection by intraseasonal sea surface temperature anomalies, *Q. J. R. Meteorol. Soc.*, *127*(573), 887–907.

Woolnough, S. J., J. M. Slingo, and B. J. Hoskins (2000), The Relationship between Convection and Sea Surface Temperature on Intraseasonal Timescales, *J. Clim.*, *13*(12), 2086–2104, doi:10.1175/1520-0442(2000).

You, Y. (1995), Salinity variability and its role in the barrier-layer formation during TOGA-COARE, *J. Phys. Oceanogr.*, *25*(11), 2778–2807.

Yu, L., and R. Weller (2007), Objectively analyzed air-sea heat fluxes for the global ice-free oceans (1981–2005), *Bull. Am. Meteorol. Soc.*, *88*(4), 527–539.

Zhang, C. (2005), Madden-Julian Oscillation, *Rev. Geophys.*, *43*, RG2003, doi:10.1029/2004RG000158.

Zhang, C., and M. J. McPhaden (2000), Intraseasonal surface cooling in the equatorial western Pacific, *J. Clim.*, *13*(13), 2261–2276.

Zhang, C., J. Gottschalck, E. Maloney, M. Moncrieff, F. Vitart, D. Waliser, B. Wang, and M. Wheeler (2013), Cracking the MJO nut, *Geophys. Res. Lett*, *40*, 1223–1230.